

Particle Size Effect of Volcanic Ash towards Developing Engineered Portland Cements

Kunal Kupwade-Patil, Ph.D.¹; Stephanie H. Chin²; Maranda L. Johnston³; Janille Maragh⁴, Admir Masic, Ph.D.⁵; and Oral Büyüköztürk, Ph.D., M.ASCE⁶

Abstract: Promoting the use of naturally available materials as a partial substitute to portland cement can be a viable solution for producing low carbon footprint and durable cements. This work assessed the chemomechanical behavior of hardened cement pastes with partial replacement of ordinary portland cement (OPC) with volcanic ash up to 50%. Volcanic ash was ground to two different mean sizes (17 and 6 μm) and then used to prepare cement–volcanic ash blends of various proportions. Mixtures were cured for 28 days; then the hardened cement paste specimens were studied for the effects of partial substitution with volcanic ash on mechanical properties, pore structure, and microstructure. The volcanic ash was engineered by decreasing the particle size, thus allowing for a greater extent of OPC replacement with volcanic ash. Strength increase was observed for specimens with up to 40% substitution of OPC with volcanic ash of a mean size of 6 μm , and this increase was attributed to the denser pore structure observed via mercury intrusion porosimetry (MIP) studies. Densification of specimens was attributed to the generation of secondary calcium silicate hydrate (C-S-H) gels when smaller-sized volcanic ash was used. This study provides a multiscale insight into engineering portland cement blends with partial replacement of portland cement with finer volcanic ash. DOI: 10.1061/(ASCE)MT.1943-5533.0002348. © 2018 American Society of Civil Engineers.

Author keywords: Volcanic ash; Portland cement; Particle size; Microcharacterization and pore characterization.

Introduction

Romans pioneered the use of crushed volcanic rocks in cements when they mixed them with limestone to build the Bay of Naples (Jackson et al. 2012; Sbordoni-Mora 1981). Historical studies have shown that the infrastructure built with volcanic ash-containing mortars in Italy has withstood extreme environments for centuries (Jackson et al. 2017). The structure of cement pastes with volcanic ash is an active area of study within the cement community; however, fewer studies have been performed on volcanic ash-blended cements than those on portland cements. The chemical reactions occurring in volcanic rocks are important, especially in

understanding the palagonitization geochemical process. Palagonitization results in the partial hydrolytic variation of sideromelane, in which basaltic glass is dissolved and hydrated, producing zeolites, smectites, and polymorphs of silica (Fisher and Schminke 1984; Pauly et al. 2011). Sideromelane consists of vitreous basaltic volcanic glass, which is commonly observed in the palagonite tuff. Palagonite is generally considered to be the replacement product of sideromelane and is usually present in the metastable state. Smectites belong to the family of phyllosilicates minerals and appear to be predominantly formed via an in situ process with the occurrence of delicate rims in detrital grains in volcanoclastic rocks (Walton et al. 2005). Due to the complexity of these chemical reactions, partial replacement of portland cement with volcanic ash remains an active area of research for cement chemists and geologists.

Significant compressive strength has been achieved with a mix of ordinary portland cement (OPC) and volcanic ash (Celik et al. 2014; Hossain 2003; Hossain and Lachemi 2006, 2007). Several factors affect the mechanical properties of cement pastes with volcanic ash such as the source of origin and variability in the chemical composition of the volcanic ash, which has been observed to influence the early age hydration of the cement paste (Husain et al. 2017; Kupwade-Patil et al. 2016b). Studies show that for fly ash with glassy phase content, smaller particle size and higher surface area directly contributed to the enhancement of the pozzolanic reaction (Chindaprasirt et al. 2005; Scrivener and Kirkpatrick 2008; Slanička 1991). Furthermore, increasing the fineness of supplementary cementitious materials (SCMs) such as fly ash was effective in increasing the gel porosity, suggesting better dispersion and packing of the finer particles. Recent studies show variability in the microstructure product formation at the early and late ages of curing (Husain et al. 2017; Kupwade-Patil et al. 2016a). Early age characterization was performed on hydrating cement paste with volcanic ash using quasielastic neutron scattering, electrochemical impedance, and Raman spectroscopy (Husain et al.

¹Research Scientist, Dept. of Civil and Environmental Engineering, Laboratory for Infrastructure Science and Sustainability, Massachusetts Institute of Technology, Cambridge, MA 02139.

²Undergraduate Researcher, Laboratory for Infrastructure Science and Sustainability, Dept. of Civil and Environmental Engineering, Massachusetts Institute of Technology, Cambridge, MA 02139.

³Undergraduate Researcher, Laboratory for Infrastructure Science and Sustainability, Dept. of Material Science and Engineering, Massachusetts Institute of Technology, Cambridge, MA 02139.

⁴Graduate Student, Laboratory for Multiscale Characterization and Materials Design, Dept. of Civil and Environmental Engineering, Massachusetts Institute of Technology, Cambridge, MA 02139.

⁵Assistant Professor of Civil and Environmental Engineering, Director of Laboratory for Multiscale Characterization and Materials Design, Massachusetts Institute of Technology, Cambridge, MA 02139.

⁶Professor of Civil and Environmental Engineering, Director of Laboratory for Infrastructure Science and Sustainability, Massachusetts Institute of Technology, Room 1-281, 77 Massachusetts Ave., Cambridge, MA 02139-4307 (corresponding author). Email: obuyuk@mit.edu

Note. This manuscript was submitted on May 2, 2017; approved on January 23, 2018; published online on June 5, 2018. Discussion period open until November 5, 2018; separate discussions must be submitted for individual papers. This paper is part of the *Journal of Materials in Civil Engineering*, © ASCE, ISSN 0899-1561.

2017; Kupwade-Patil et al. 2016b; Masmoudi et al. 2017). These studies highlighted the effect of particle size and concentration of volcanic ash on free and chemically bound water during the early stage of hydration. Moreover, grinding the ash increased the extent of pozzolanic reaction as additional calcium silicate hydrate (C-S-H)-related phases were formed in the hydrating cement paste. Pozzolanic reaction not only depends on the chemical composition of the natural pozzolana (volcanic tuff) but also on the length and temperature of curing (Massazza 2002). Further studies using differential scanning calorimetry (DSC) for evaluating hydration rates along with small-angle scattering are required to examine the structure of the resulting hydration products. Densification in hardened cement pastes prepared with volcanic ash was attributed to formation of C-S-H and calcium aluminosilicate hydrate (C-A-S-H) gels, while the development of magnesium silicate hydrate (M-S-H) led to decalcification of C-S-H and C-A-S-H gels, which resulted in an increase in porosity of the cementitious matrix (Kupwade-Patil et al. 2016a). Thus, volcanic ash as a precursor material needs to be engineered before being mixed with OPC to facilitate uniform hydration, which initializes pozzolanic reactions within the cement paste.

The objective of this study was to examine the chemomechanical behavior of hardened cement pastes when OPC was partially replaced by up to 50% of two different sizes of volcanic ash. Commercially available volcanic ash was mechanically ground to a finer size allowing for more extensive substitution of OPC with volcanic ash. Mechanical testing of 28-day-cured specimens was accompanied by microstructure and pore structure analyses from the nano- to micrometer scale using several techniques. Backscattered electron microscopy (BSE) images were in the range of micrometer scale with the energy-dispersive spectrum (EDS) analysis detecting the chemical composition, synchrotron X-ray diffraction (XRD) analysis revealing the nanocrystalline phases, and Raman spectroscopy detecting phase in the nano- to micrometer range, while pore structure was determined via mercury intrusion porosimetry (MIP) studies in the nano- to micrometer range. The mechanical analysis by evaluating compressive strength was determined in megapascals using samples that were in the millimeter-length scale.

Materials and Methods

Raw Material Analysis

Volcanic ash from the Kingdom of Saudi Arabia (KSA) was procured from the Pozzolan Product Factory in Jeddah, KSA. The volcanic ash distributed commercially by the manufacturer had a mean size diameter of 17.14 μm . This volcanic ash as produced by the manufacturer (VA) was ground to an even smaller sized volcanic ash (GVA) using a high-speed vibratory ball mill. The particle size distributions (PSDs) of OPC, the VA as received from the manufacturer, and the GVA were measured using a laser-based particle size analyzer (Fig. 1). The average means, medians, and modes of the diameters and the diameters at select volume percentiles for these three materials are shown in Table 1. The VA and GVA had mean particle sizes of 17 and 6 μm , respectively. The main objective of this work was to examine the effect of reduction in mean particle size of the volcanic ash on chemical, mechanical, and morphological features of the cement paste.

Chemical analysis of volcanic ash and portland cement was performed using an energy-dispersive X-ray fluorescence (EDXRF) spectrometer. An electrically cooled silicon drift detector with a 30×1 mm active area, an 8.8-mm 50-kV X-ray beam collimator, and a 50-W rhodium target X-ray tube were used for this

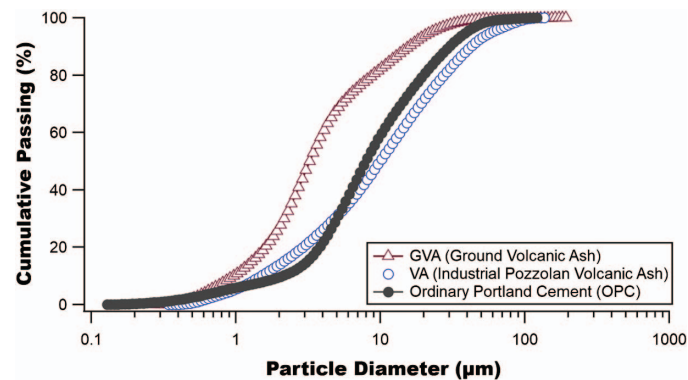


Fig. 1. (Color) Particle size distribution analysis for volcanic ashes (VA = volcanic ash as received by the manufacturer and GVA = finely ground volcanic ash) and OPC.

experiment. The X-ray fluorescence (XRF) analysis provided the mass percent distribution of oxides (Table 2). The total proportion of silicon oxide (SiO_2), aluminum oxide (Al_2O_3), and ferric oxide (Fe_2O_3) components for the raw volcanic ash was 74.3%.

Mixing and Curing of Samples

The samples were cast as per ASTM C305 (ASTM 2014). Initial dry mixing of volcanic ash and OPC was performed using a Daigger (Bohemia, New York) Vortex-Genie 2 blender at 3,200 rpm for 1–2 min to ensure a uniform distribution of volcanic ash and portland cement. Then water was slowly added while continuously mixing until a water-to-cement ratio of 0.35 was achieved, and when the water was fully incorporated the mixture was poured into molds. As per ASTM C109 (ASTM 2016), 50-mm (2-in.) cubic specimens were batched for compression testing. For the samples to be tested in compression, the cement paste was tamped after pouring. Three specimens were prepared for each blend of volcanic ash and OPC. After 24 h of curing in the mold, the specimens were demolded and were submerged in lime water and cured at $20 \pm 3^\circ\text{C}$ for 28 days, after which the samples were immersed in pure acetone for 1–2 days to retard the hydration. The samples were immediately tested after removal from the acetone solution.

Each sample was labeled based on the mean particle size category and the corresponding weight percentage of the volcanic ash. For example, a sample with 30% composition by weight 17- μm VA and 70% by weight OPC is referred to as VA-30; similarly, a sample with 30% by weight 6- μm GVA and 70% by weight OPC is referred to as GVA-30 (Table 3).

Methods

Mechanical testing was performed using compression test analysis as per ASTM C109 (ASTM 2016). The chemical composition of the volcanic ashes and OPC was studied via XRF and PSD, performed using a laser-based particle size analyzer. Microstructure characterization included BSE and energy dispersive spectrum (EDS), synchrotron X-ray diffraction, and Raman spectroscopy. Pore structure studies were performed using MIP (Table 4).

The following sections summarize the experimental methods used for characterization at multiple length scales to provide insight into the microstructure and pore structure of cement-based materials. These techniques can provide insight into the effect of particle size and proportion of volcanic ash on the properties of hardened cement pastes, in which volcanic ash was used as a partial substitute for portland cement.

Table 1. Particle size analysis with two different particle sizes

Binder type	Nomenclature	Mean (μm)	Median (μm)	Mode (μm)	Diameter for selected percentiles by volume		
					D_{90} (μm)	D_{50} (μm)	D_{10} (μm)
Volcanic ash	VA	17.14	10.00	13.27	42.46	10.00	1.50
Volcanic ash	GVA	6.00	3.25	2.977	15.79	3.25	0.97
Portland cement	OPC	12.73	7.94	6.65	30.10	7.94	2.12

Table 2. X-ray fluorescence spectroscopy of portland cement and volcanic ash

Binder type	Mass percent as oxide									
	CaO	SiO ₂	Al ₂ O ₃	MgO	SO ₃	TiO ₂	K ₂ O	Fe ₂ O ₃	Na ₂ O	P ₂ O ₅
OPC	62.80	20.1	4.140	1.58	2.35	0.20	0.65	3.17	0.12	0.11
VA	9.29	47.0	14.80	7.95	—	2.41	1.40	12.5	3.54	0.61
GVA	9.28	47.1	14.90	7.97	—	2.41	1.39	12.30	3.55	0.60

Note: VA = volcanic ash with mean particle size of 17 μm ; and GVA = volcanic ash with mean particle size of 6 μm .

Table 3. Composition of volcanic ash and OPC

OPC (%)	VA (%)	GVA (%)	Nomenclature
100	0	0	OPC
50	50	0	VA-50
60	40	0	VA-40
70	30	0	VA-30
80	20	0	VA-20
90	10	0	VA-10
50	0	50	GVA-50
60	0	40	GVA-40
70	0	30	GVA-30
80	0	20	GVA-20
90	0	10	GVA-10

Note: VA = volcanic ash with a mean size of 17 μm ; and GVA = volcanic ash with a mean size of 6 μm .

Mechanical Testing

Compression testing provided direct information on the bulk strength among other material characteristics, which can be qualitatively related to its strength (Neville 2011). The cubic specimens were subjected to compression testing as per ASTM C109 at loading rate of 0.72 mm/min. For each sample type, the compressive strengths for the three specimens were measured and averaged. The average compressive strength was reported to the nearest 0.1 MPa.

BSE Imaging and EDS analysis

BSE imaging was performed on polished samples to understand the additive's effect on the structure and chemistry of the cementitious matrix. First, the samples were cast in epoxy and polished to 50-nm surface roughness. The cylindrical polished samples were 38 mm in diameter and 15 mm in depth. The polishing procedure involved a sequence of polishing stages for various lengths of time at applied forces, outlined in Table 5. A field-emission scanning electron microscope (FE-SEM) was used to carry out the BSE analysis. EDS elemental and phase mapping were also carried out on these samples.

The oxide composition obtained through EDS was analyzed using ternary phase diagrams. Ternary phase diagrams are commonly used in metamorphic geology for visualizing and predicting relative phase contents from three variables (Herfort and Lothenbach 2015). This study used two types of ternary (three-variable) diagrams: CaO-Al₂O₃-SiO₂ and MgO-Al₂O₃-SiO₂. Phase quantification in terms of medium- and high-calcium content was calculated based on the standard ternary phase diagrams (Garcia-Lodeiro et al. 2011; Krauskopf and Bird 1995).

Synchrotron XRD Analysis

Powdered samples were studied using synchrotron radiation on Beamline 11-BM, a powder diffractometer at the Advance Photon Source, Argonne National Laboratory, Lemont, IL. The advantages

Table 4. Experimental techniques used this work for microstructure, pore structure, and mechanical characterization

Characterization technique	Category	Sample type	Parameters and metrics (units)
XRF spectroscopy	Chemical analysis	Powder (OPC and volcanic ashes)	Oxide composition (%)
Particle size analysis	Microstructure	Powder (OPC and volcanic ashes)	Particle size measured for mean, median, and mode (μm)
Compressive strength	Mechanical properties	Solid	Compressive strength (MPa)
Synchrotron XRD	Microstructure	Powder	Phase analysis
BSE	Microstructure	Solid sample (polished)	Morphology and structure
EDS analysis	Microstructure and chemical analysis	Solid sample (polished)	Elemental analysis and data analyzed using ternary phase diagrams
Raman spectroscopy	Microstructure and chemical analysis	Solid sample	Raman shift (cm^{-1}); phase analysis and bonding information
MIP	Pore structure analysis	Solid sample	Porosity (%) and threshold pore diameter (μm)

Table 5. Polishing procedure for backscattered electron spectroscopy imaging

Grit	Time (min)	Force [N (lb)]
120	4	26 (6)
240	4	26 (6)
320	8	26 (6)
400	8	26 (6)
600	8	26 (6)
800	16	26 (6)
1,200	30	26 (6)
9 μm	120	35 (8)
3 μm	60	40 (9)
1 μm	60	40 (9)
0.25 μm	60	40 (9)
0.1 μm	30	40 (9)

of using synchrotron XRD over laboratory XRD equipment are as follows (Wang et al. 2008):

- The shorter wavelength of the synchrotron X-ray beam provides greater structural information on the sample by enabling more observations over a wider scattering vector (\mathbf{Q}) range (especially for smaller d -spacing).
- Compared with common laboratory radiation sources, the shorter wavelength used at synchrotron-based XRD greatly reduces or eliminates fluorescence problems for most samples.
- The extremely high-flux and high-resolution data allow more peaks to be resolved, which is essential for correct pattern indexing.
- The higher operating energy generally reduces sample absorption. This enables the use of transmission geometry diffraction for nearly all samples, even those containing high-Z elements.

For this instrument, a double Si(111) monochromator extracts a monochromatic beam from the white beam. The sample was ground to a fine powder (grain size = 1–10 μm) and introduced in a Lindeman tube ($F = 0.3$ mm). The sample was rotated around the capillary axis to reduce preferred orientation problems inherent to such layered compounds. X-rays of wavelength 0.04142 nm (0.4142 Å) and a fixed energy of 30 keV were used.

Raman Spectra Analysis

Raman spectroscopy can identify phases by detecting specific covalent chemical bonds. When spectra are found to contain characteristic peaks, these peaks can be associated with covalent bonds present in known phases in order to identify mineral phases in the specimen. Raman spectra were collected for the specimens using a WITec (Ulm, Germany) alpha300 R confocal Raman microscope system with a diode laser of excitation wavelength of 532 nm and a grating of 600 L/mm. The detector connected to the system was a thermoelectrically cooled and charge-coupled device (CCD) camera (DU401A-BV, Andor, Belfast, UK). A specific spot on the solid sample was obtained at the optical magnification of 50 \times . The system used profilometry to measure the topography of the unpolished sample. The system then used the measured topography of the sample to translate the stage in three directions during large area scanning to maintain confocality. The longitudinal shape of the laser aided in covering a more representative area under the laser spot size in order to overcome the inherent heterogeneity of the materials under study. Nonnegative matrix factorization (NMF) was used to obtain the individual phases present in each sample from the set of all Raman spectra recorded for that sample. The set of all Raman spectra for each sample was also used to obtain an

average spectrum for each sample, which indicated all the phases recorded over the area measured.

Pore Structure Analysis

The pore structure was characterized using MIP, which is able to track pores in the range from 0.01- μm to 1-mm diameter. This broad pore size distribution helped to assess the effects of the additives on the densification of the cementitious matrix. A solid portion of sample (5 × 2 × 5 mm) was extracted from all the samples, and MIP was performed on each sample portion using a Micromeritics (Norcross, Georgia) Autopore V 9600 at a peak pressure of 230 MPa, an advancing contact angle of 138°, and a receding contact angle of 128°.

Porosity of the specimen was calculated as

$$\text{Porosity}(\%) = \frac{100 \times V_{\text{total}}}{V_b} \quad (1)$$

where V_b = bulk volume; and V_{total} = total mercury intrusion volume.

The bulk volume (V_b) is calculated by $V_b = V_p - V_m$, where V_p = user-entered volume for the penetrometer, and V_m = volume of mercury in the penetrometer.

Results and Discussion

Mechanical Test

Compression strength test studies were performed on all samples as per ASTM C109 (ASTM 2016). The compressive strengths in megapascals for all samples are shown in Fig. 2. The GVA-30 sample prepared with 6- μm -sized volcanic ash showed the highest strength (63.4 MPa), whereas VA-10 showed the least strength (34.44 MPa). For both sample types—VA and GVA—compressive strength increased with the amount of volcanic ash additive for up to 30% substitution of OPC, but there was a marginal decrease in strength for 40% or more of volcanic ash. This suggests an optimal mix is to replace 30% of the OPC with volcanic ash of an average particle size of 6 μm , and that substituting more than 30% of the OPC would decrease the strength of the hardened cement paste.

The strength behavior in cement pastes is attributed to the evolution of microstructures during hydration, which control the gel-to-space ratio in the cement pastes. When dealing with complex cement mixtures, the bulk compressive strength values are

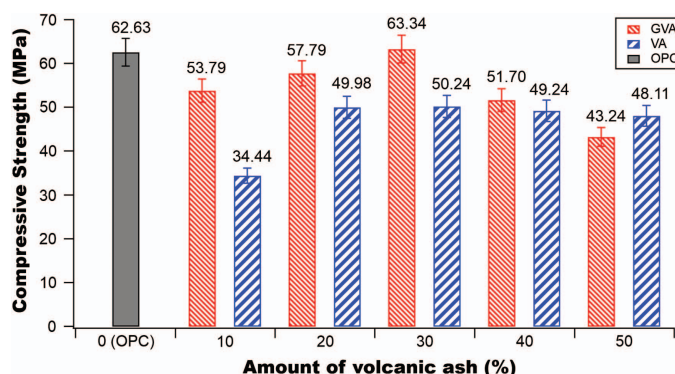


Fig. 2. (Color) Compressive strength for OPC and OPC–volcanic ash samples with two different particle sizes. GVA = mean particle size of 6 μm ; and VA = mean particle size of 17 μm .

necessary. However, they do not indicate a complete understanding of why an increase or decrease in strength was observed. Hence, the current study utilizes characterization techniques at multiple length scales to understand which hydration products contribute to increased strength when portland cement is partially replaced by volcanic ash.

BSE Imaging and EDS Analysis

BSE micrographs of the VA-50 and GVA-50 samples are shown in Fig. 3, and their elemental maps are shown in Figs. 4 and 5, respectively. EDS elemental mapping shows Si- and Mg-rich phases that have been related to Mg–Si phyllosilicates. Iron-rich zones were observed in GVA-50 samples due to the high proportion of iron

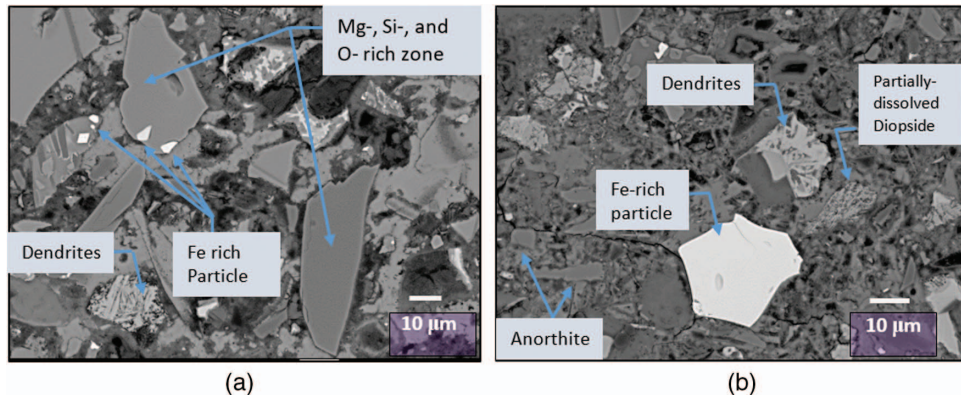


Fig. 3. (Color) BSE images of polished samples of (a) VA-50; and (b) GVA-50.

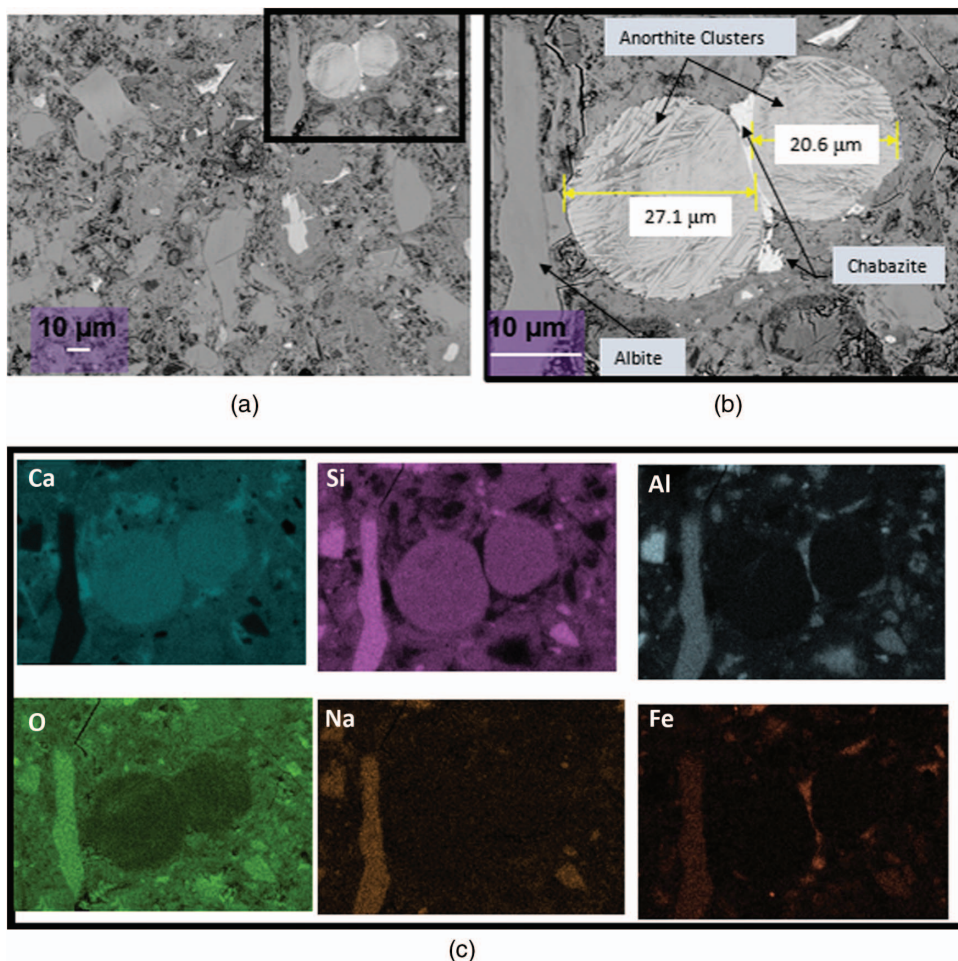


Fig. 4. (Color) BSE image of GVA-50 specimen: (a) image at 500× magnification showing unreacted volcanic ash inside the hardened cement paste; (b) magnified image showing zeolithic crystal growth inside the unreacted volcanic ash; and (c) EDS elemental distribution maps for Ca, Si, Al, O, Na, and Fe.

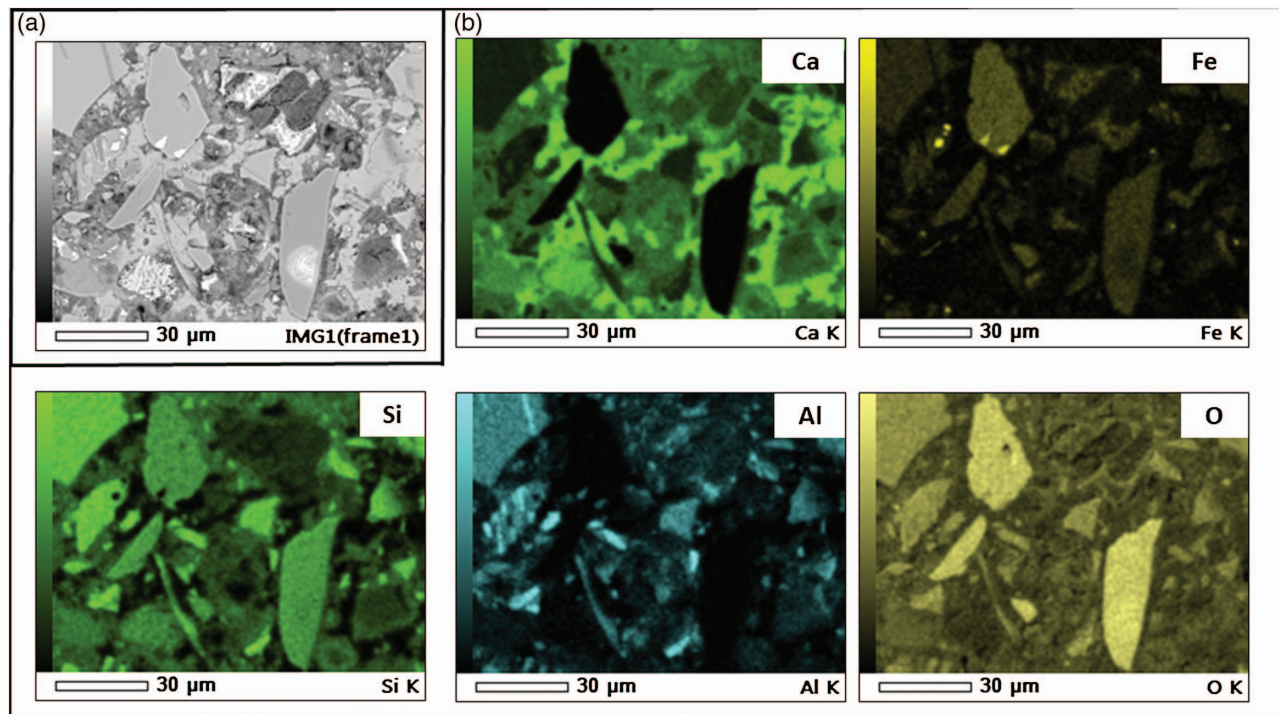


Fig. 5. (Color) (a) BSE image of VA-50 specimen; and (b) EDS mapping of VA-50 specimen for Ca, Fe, Si, Al, and O.

content in the volcanic ash. Bifurcation of phases rich in iron and alumina-silica occur within the volcanic ash particle or at the interface of the unreacted ash particle, resulting in traces of insoluble iron-rich dendritic particles (Gardner et al. 2015; Lloyd et al. 2009) (Fig. 3).

The VA-50 and GVA-50 specimens showed the presence of dendrite structures of partially dissolved diopside ($MgCaSi_2O_6$) [Figs. 6(a and b)]. Plagioclase and fibro-palagonite from the unreacted volcanic ash were detected as a darker region [Fig. 6(b)]; their presence reflects that the close interaction of the gel-palagonite and fibro-palagonite inside the pore structure leads to the precipitation of dissolved species in the alkali-rich environment. Studies have shown that fibro-palagonite is less reactive with pozzolans than gel-palagonite (Celik et al. 2014; Moon et al. 2014). However, in the current work, it was difficult to distinguish these two phases due to the complexity of the resulting microstructure.

The BSE image of the unreacted volcanic ash within the samples showed anorthite clusters [$Ca(Al_2Si_2O_8)$] as round crystals

with uniform twin clusters and lath-shaped grains (Fig. 4). The Al-rich chabazite phase was detected at the rim of the anorthite clusters. The elemental analysis via EDS shows that anorthite crystals were rich in Ca, Si, and O and contained traces of Al, whereas albite feldspar crystals were rich in Al, Na, and O [Fig. 4(c)].

A $CaO-Al_2O_3-SiO_2$ ternary phase diagram for all samples is shown in Fig. 7. The oxide compositions were determined using EDS data from the polished specimens and plotted on a ternary phase diagram to examine the phases. VA-10 and VA-30 lay in the high-calcium zone, whereas the rest of the VA samples were in the medium-calcium zone. As detected via XRD analysis, the high calcium content zone is related to the high-calcium C-A-S-H gels and the presence of crystalline phases such as chabazite-Ca. VA-50, VA-40, GVA-50, and GVA-40 had higher traces of aluminum, and therefore showed traces of hydrogarnets such as wairakite (Fig. 7).

Almost every specimen with high Ca content (including OPC, VA-30, and GVA-30, but not VA-10) had higher strengths than

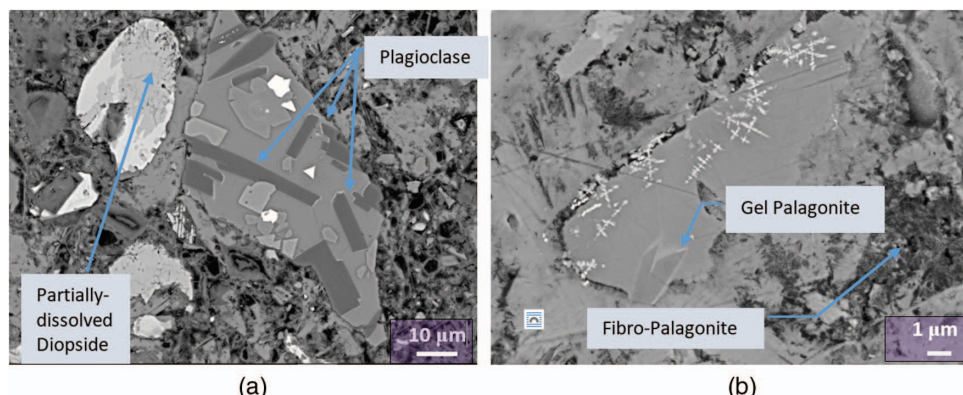


Fig. 6. (Color) BSE image of polished samples of (a) VA-50; and (b) GVA-50.

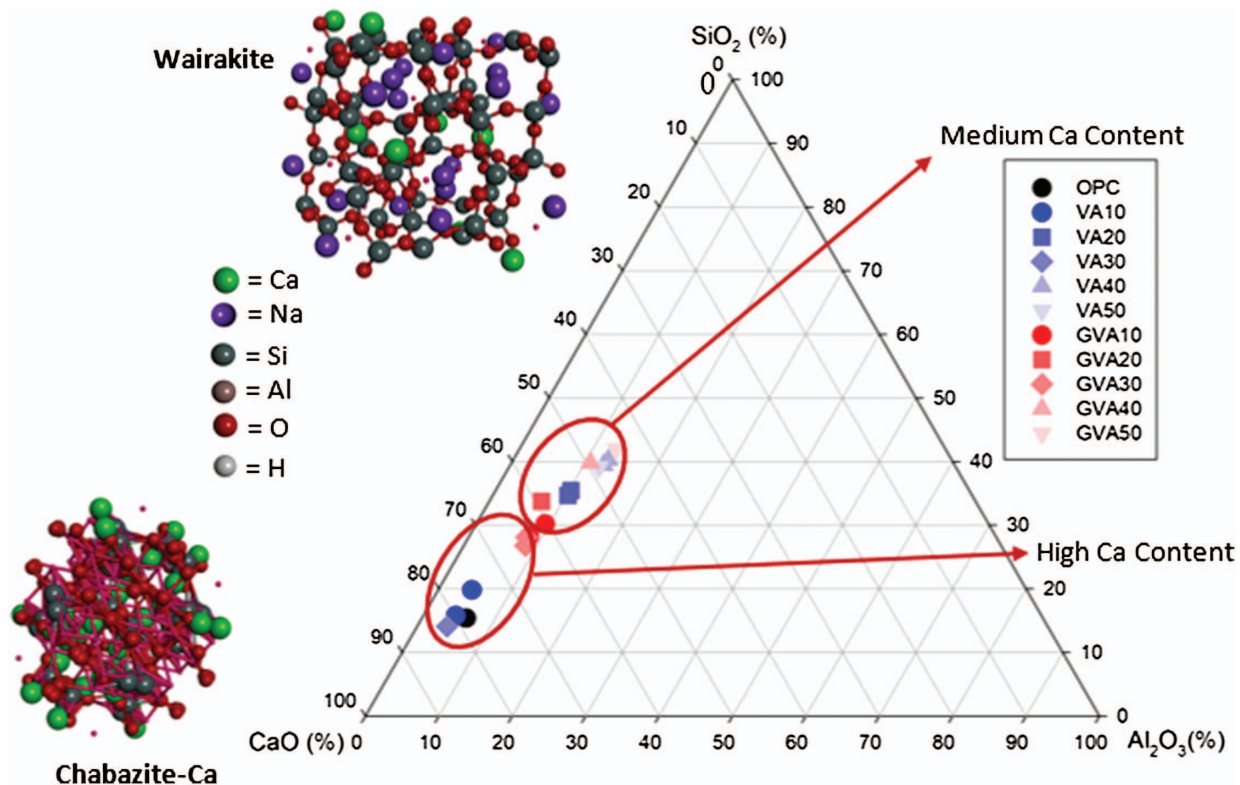


Fig. 7. (Color) Ternary phase diagram ($\text{CaO}-\text{SiO}_2-\text{Al}_2\text{O}_3$) from EDS analysis.

specimens with lower Ca content with approximately less than 60% CaO (GVA-50, GVA-40, VA-40, and VA-50). GVA-10, GVA-20, and GVA-30 showed significantly greater strengths, medium calcium contents, and lower free-Al contents than their corresponding VA samples, which indicates that grinding the volcanic ash from 17 to 6 μm decreased the amount of calcium used to form high-calcium hydration phases and increased the amount of alumina used to form high-Al hydration phases. The high calcium content zones were related to high-density C-S-H gel, whereas medium calcium content zones were dominated by high-alumina C-A-S-H gel, which suggests that the C-S-H phase was primarily responsible for the increased strength. Previous studies have shown that strength in cement pastes prepared with natural pozzolana (volcanic ash) increases as the amount of combined lime is increased (Massazza 2002). Uncombined lime in the paste decreases by increasing the natural pozzolana content in the mix. The addition of volcanic ash increases the alumina, calcium, and silica in the mix, and it may have led to the formation of secondary C-S-H due to the pozzolanic reaction with the available calcium hydroxide. Natural pozzolans of volcanic origin (pumices, volcanic ash, and zeolite tuffs) experience mass loss and lose chemically bound water at relatively low temperatures ($\sim 200^\circ\text{C}$) (Bernal et al. 2016; Snellings et al. 2012). Additionally, grinding the volcanic ash to a finer particle size increases the extent of the pozzolanic reaction and thus the conversion of free water to chemically bound water (Kupwade-Patil et al. 2016b). Further in situ studies are required to examine the hydration products and relate them to the heat of hydration using thermal calorimetry.

The effect of magnesium oxide content on phase development was examined using a $\text{MgO}-\text{SiO}_2-\text{Al}_2\text{O}_3$ ternary phase diagram (Fig. 8). OPC, VA-10, and VA-30 showed the presence of mullite ($3\text{Al}_2\text{O}_3 \cdot 2\text{SiO}_2$) along with traces of tridymite and cristobalite. VA-30, VA-40, and VA-50 displayed traces of cordierite

($2\text{MgO} \cdot 2\text{Al}_2\text{O}_3 \cdot 5\text{SiO}_2$), whereas GVA-30, GVA-40, and GVA-50 were dominated by the presence of enstatite (MgSiO_3). Cordierite and other types of feldspar were observed due to the unreacted volcanic ash. Cordierite and mullite are formed at $1,350^\circ\text{C}$. The low strength due to the presence of cordierite is usually compensated by the presence of mullite (Hipedinger et al. 2002). Cordierite possesses an advantage in terms of low thermal expansion and high thermal shock resistance; it is therefore used for building durable refractory ceramics (Sorrell 1960).

GVA-30, GVA-40, and GVA-50 specimens showed traces of enstatite (MgSiO_3), which is related to an M-S-H phase. At the high temperature of $850\text{--}950^\circ\text{C}$, phyllosilicate sheets in talc [$\text{Mg}_3\text{Si}_4\text{O}_{10}(\text{OH})_2$] undergo dihydroxylation and break down into SiO_2 and enstatite, which are common components of volcanic materials (Leonelli et al. 2007; Nied et al. 2016). Enstatites form lath-shaped crystals and appear as dark regions, as shown in the BSE micrograph in Fig. 4. The presence of these crystalline magnesium silicate (enstatite) and magnesium aluminosilicate (cordierite) phases, which can be found in volcanic ash, suggests that these phases were not fully involved in the hydration reaction between volcanic ash and OPC. Thus, a lower strength in samples with greater than 30% replacement of OPC might be attributed to the unreacted enstatite and cordierite phases.

XRD Analysis

XRD data collected at wavelength of 0.04142 nm (0.4142 \AA) for OPC, VA, and GVA specimens are shown in Figs. 9–11, respectively. The OPC specimen showed peaks of cristobalite [International Centre for Diffraction Data (ICDD): 00-039-1425], portlandite (ICDD: 00-001-1079), calcium silicate hydrate (C-S-H II) (ICDD: 00-029-0374), ettringite (ICDD: 00-013-0350), gibbsite (ICDD: 00-001-0263), and calcite (ICDD: 00-001-0837) (Fig. 9). The C-S-H II and gibbsite phases are credited from past

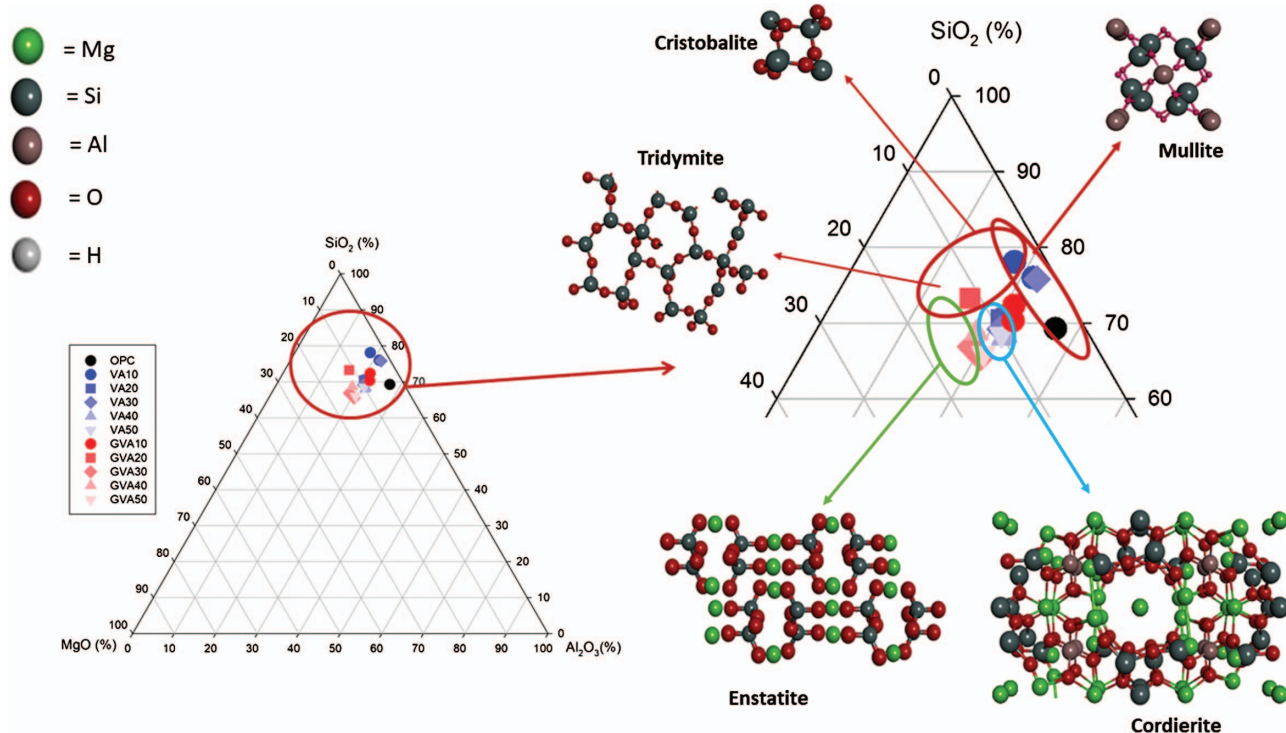


Fig. 8. (Color) Ternary phase diagram ($\text{MgO}-\text{SiO}_2-\text{Al}_2\text{O}_3$) from EDS analysis.

studies as strength enhancement phases in portland cement paste (Hewlett 2003; Taylor 1997). Cristobalite, portlandite (crystalline form of calcium hydroxide), ettringite, and calcite have been observed in OPC.

The XRD analysis for VA-10, VA-30, and VA-50 is shown in Fig. 10. As the percentage of volcanic ash increased, the alumina and magnesium content increased in the mix, and thus VA-10 and VA-50 had chabazite-Ca present, whereas VA-30 and VA-50 showed the presence of tobermorite. Furthermore, ettringite was detected in VA-30 and VA-50, and calcium sulfate hydrate was detected in all three samples.

VA-30 and VA-50 showed the presence of tobermorite, whereas VA-10 did not show any trace of tobermorite, which is related to the C-S-H phase. On the other hand, chabazite-Ca, which was found in

VA-10 and VA-50 but not VA-30, is a zeolitic phase commonly related to the crystalline form of the C-A-S-H phase. VA-50 and VA-30 had higher strength phases than VA-10, which suggests that the C-S-H phase contributes to high strength more than the C-A-S-H phase (Puertas et al. 2011). Furthermore, due to the addition of volcanic ash, dolomite was observed in the VA-10 and VA-50 specimens and brucite was detected in the VA-30 and VA-50 samples. Studies have shown that these phases can react with available calcium hydroxide to form magnesium silicate hydrates, which are considered to be less stable, and to lower the compressive strength of the specimen (Brew and Glasser 2005; Zhang et al. 2014).

XRD spectra for specimens prepared with 6- μm GVA at 10, 30, and 50% substitution of portland cement with volcanic ash are shown in Fig. 11. Calcite and C-S-H II were observed in the

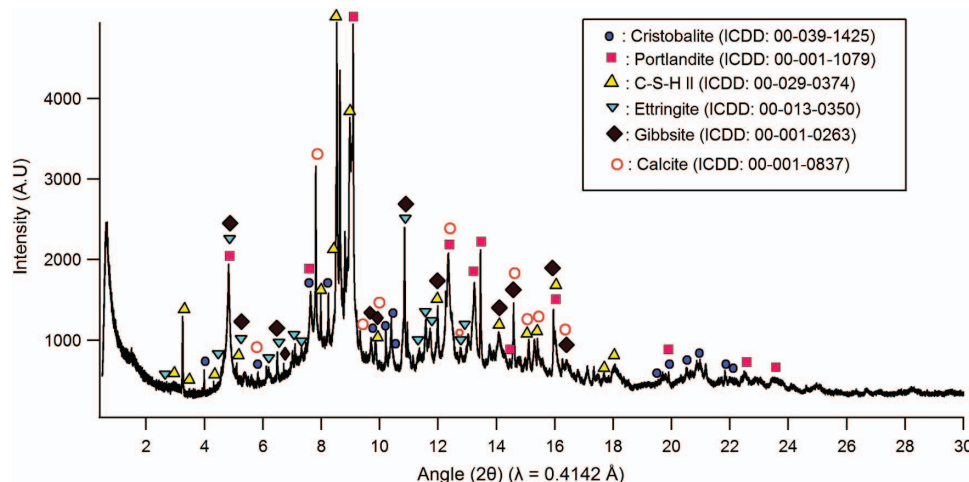


Fig. 9. (Color) Synchrotron XRD data obtained at wavelength of 0.414 \AA for ordinary portland cement paste after 28 days of hydration.

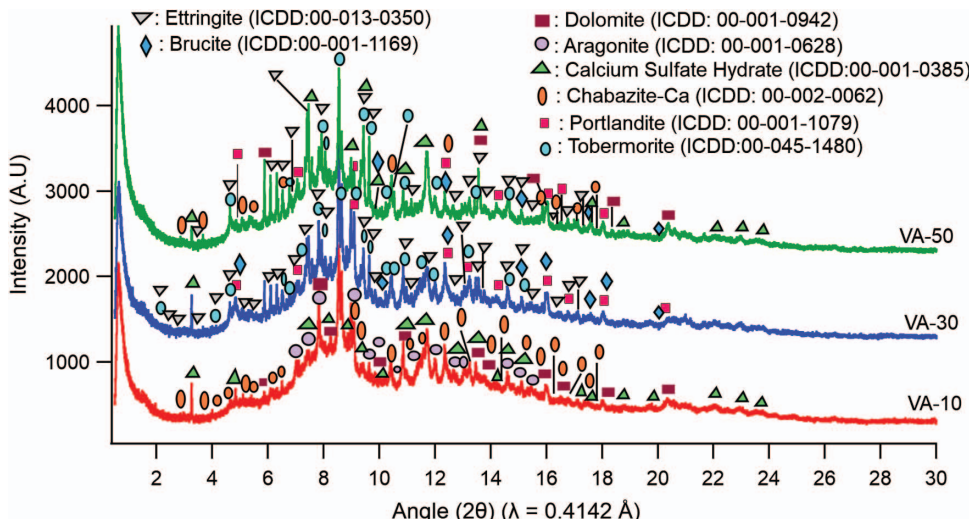


Fig. 10. (Color) Synchrotron XRD data for 28-day cured cement pastes prepared with OPC and 17- μm VA at wavelength of 0.414 \AA .

GVA specimens, but not in the VA counterparts. Studies have shown that the presence of portlandite along with C-S-H is responsible for higher compressive strength (Mindess 2000; Skalny et al. 2001). Additionally, grinding the volcanic ash from 17 to 6 μm may have helped in allowing the portlandite to react with the aluminosilicates, which may have led to the formation of secondary C-S-H. Calcite does not predominantly affect the C-S-H phase; however, it can fill pore space more effectively when it reacts with the Al_2O_3 - Fe_2O_3 -tri (AFt) phase (Matschei et al. 2007). Rosenhahnite was found in all three GVA samples, suggesting the presence of unreacted volcanic ash that was not involved in the initial hydration reaction. Rosenhahnite forms at ambient conditions at unstable high temperatures in aluminosilicate products such as volcanic ash (Bayuseno and Schmahl 2010). Rosenhahnite contains linear groups of three silica tetrahedral; the two outer silicon atoms each share a common oxygen with the silicon in the center (Alper 2012). This structure does not contain molecular water; however, the hydroxyl groups are attached to the outer silicon atoms. Brucite along with

hydrotalcite [$\text{Mg}_6\text{Al}_2\text{CO}_3(\text{OH})_{16} \cdot 4(\text{H}_2\text{O})$] was detected among GVA specimens (Fig. 11). Formation of hydrotalcite requires the diffusion of aluminum, which could be provided by the volcanic ash. It has been reported that hydrotalcite could be intimately mixed with C-S-H and AFm (Al_2O_3 – Fe_2O_3 – mono) phases (Barker 1989).

Volcanic ash had an Al_2O_3 content of 14.90%, and Luke et al. (1981) showed that cement mix with greater than 8% Al_2O_3 leads to the formation of wairakite and Si-rich hydrogarnets. Additionally, wairakite is responsible for controlling the solubility of Al and Si and belongs to the zeolite group along with chabazite-Ca, which was detected in all three GVA samples as shown in Fig. 11 (Engelsen et al. 2009).

GVA-10 and GVA-30 showed significantly higher strength than VA-10 and VA-30 specimens (Fig. 2), and this can be attributed to the formation of C-S-H and C-A-S-H phases. XRD analysis indicates that the presence of tobermorite and C-S-H II (plumbierite) are assigned to the C-S-H phase, while chabazite-Ca and waikarite

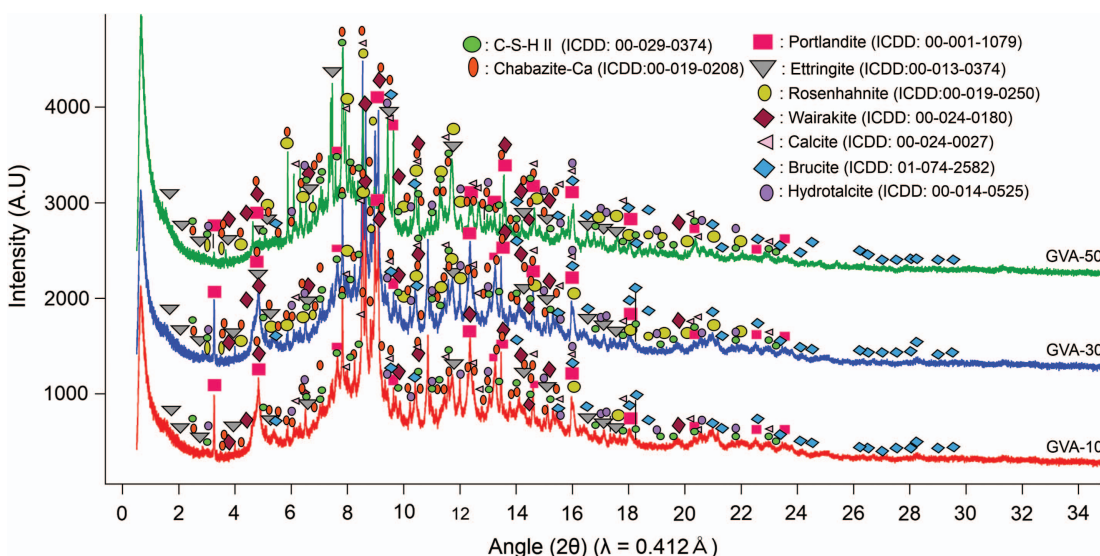


Fig. 11. (Color) Synchrotron XRD data for 28-day cured cement pastes prepared with OPC and 6- μm GVA at wavelength of 0.4142 \AA .

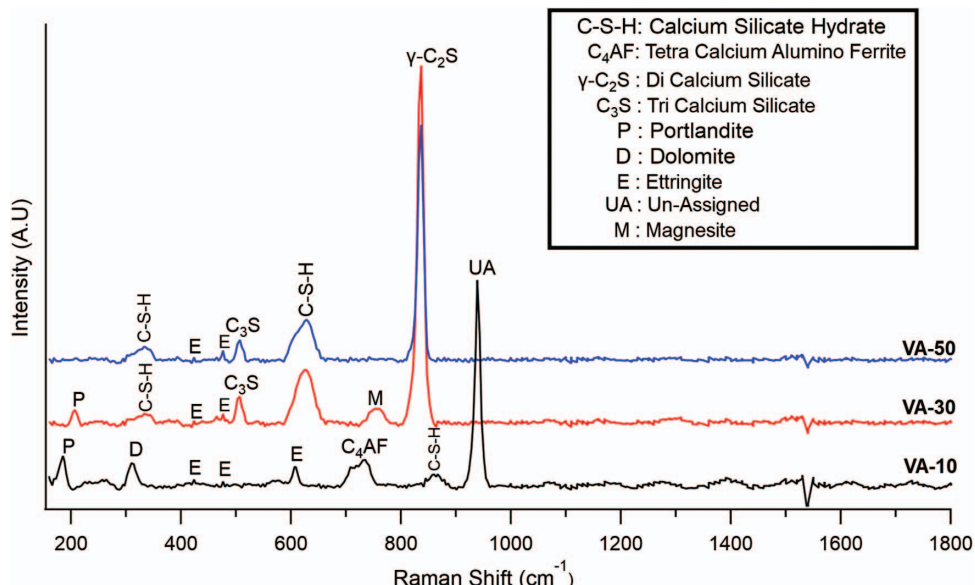


Fig. 12. (Color) Raman spectra analysis with 10, 30, and 50% replacement of OPC with 17- μm VA.

are assigned to the crystalline C-A-S-H gel phases. The specimens with the combination of C-S-H and C-A-S-H gel showed higher strength when compared with the only C-A-S-H gel dominated specimen (VA-10). This supports that C-S-H is the main ingredient for strength enhancement, while C-A-S-H gel alone cannot significantly contribute to strength enhancement. Along with C-S-H-related phases, a significant amount of calcite was observed among GVA samples. Studies have suggested that calcite along with C-S-H could improve the early strength by forming a dense pore structure (Matschei et al. 2007; Skalny et al. 2001), but the role of calcite during the hydration process is an ongoing area of research, and further studies are necessary to examine whether calcite functions as an active hydration reactant or as an inert filler when both volcanic ash and pure calcite are involved in the hydration process.

Raman Spectra Analysis

Raman spectra for 10, 30, and 50% substitution of volcanic ash prepared with 17 and 6 μm are shown in Figs. 12 and 13, respectively. Phases of portlandite (185 and 204 cm^{-1}) were observed among VA-10 and VA-30 specimens, and Si-O-Si bonds of the C-S-H gel were detected at 336 and 645 cm^{-1} . The VA-10 specimen showed a strong peak at 939 cm^{-1} , which was unassigned. Strong peaks of γ -C₂S at 873 cm^{-1} and intermediate peaks of C₃S at 520 cm^{-1} were detected on VA-30 and VA-50 specimens (Fig. 12). Additionally, a γ -C₂S peak was observed for GVA-30 and GVA-50 specimens; however, C₃S peaks were not present among GVA samples (Fig. 13). This clearly suggests that grinding the volcanic ash from 17 to 6 μm indicated that C₃S was involved in the formation of the C-S-H- and C-A-S-H-related phase among GVA specimens.

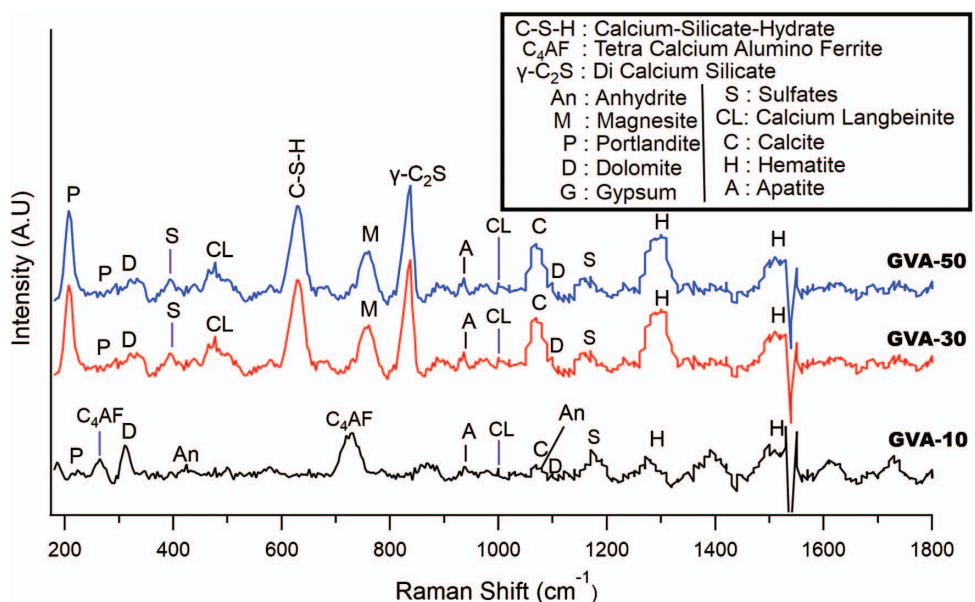


Fig. 13. (Color) Raman spectra analysis with 10, 30, and 50% replacement of OPC with 6- μm GVA.

A broad spectra that is related to phases with higher Al-to-Fe ratios such as calcium aluminoferrite (C_4AF) was visible at 750 cm^{-1} for both VA-10 and GVA-10, as shown in Figs. 12 and 13, respectively (Conjeaud and Boyer 1980). The addition of volcanic ash increased the calcium, sulfur, and magnesium content in the mix, leading to the formation of calcium langbeinite and magnesite for 30 and 50% replacement of OPC with both 17- and $6\text{ }\mu\text{m}$ volcanic ash. GVA specimens showed phases of hematite associated with broad peaks between the ranges of $1,260\text{--}1,330\text{ cm}^{-1}$ and $1,460\text{--}1,540\text{ cm}^{-1}$ (Fig. 13). These peaks were absent for the VA samples as shown in Fig. 12. Unreacted hematite may be responsible for the lower strength found in GVA-50 and GVA-10 compared with GVA-30 because it does not contribute to strength and instead remains unreacted in the matrix. In addition, strong peaks of portlandite were present in the GVA-50, but not VA-50. This indicates that grinding the volcanic ash from 17 to $6\text{ }\mu\text{m}$ can lead to the presence of portlandite, which may contribute to the formation of secondary C-S-H. Therefore, for each GVA sample of 20% or greater volcanic ash content, the GVA specimen showed higher strength than its VA counterpart.

Mercury Intrusion Porosimetry

MIP was used to analyze the pore structure and porosity of the samples after 28 days of hydration. Threshold pore diameters, which are defined as the largest pore diameter at which significant intruded mercury pore volume is detected (Diamond 2000), were calculated to be the pore size at the first inflection point, as demonstrated in Fig. 14. Threshold pore diameter provides vital information regarding the connectivity of the pore network.

Threshold pore diameters for all the specimens are shown in Fig. 15. VA-10 had the highest threshold pore diameter (226 nm), while GVA-20 had the smallest pore diameter (70 nm) of all the samples. In general, GVA samples had not only higher strength, but also smaller threshold pore diameters than their VA counterparts. By increasing the concentration of $6\text{-}\mu\text{m}$ volcanic ash from 10 to 20%, the threshold pore diameter dropped by $\sim 35\%$. For $17\text{-}\mu\text{m}$ volcanic ash, there was a marginal decrease in the pore diameter with increasing VA for up to 30% substitution of OPC with VA and then a marginal increase in pore diameter with

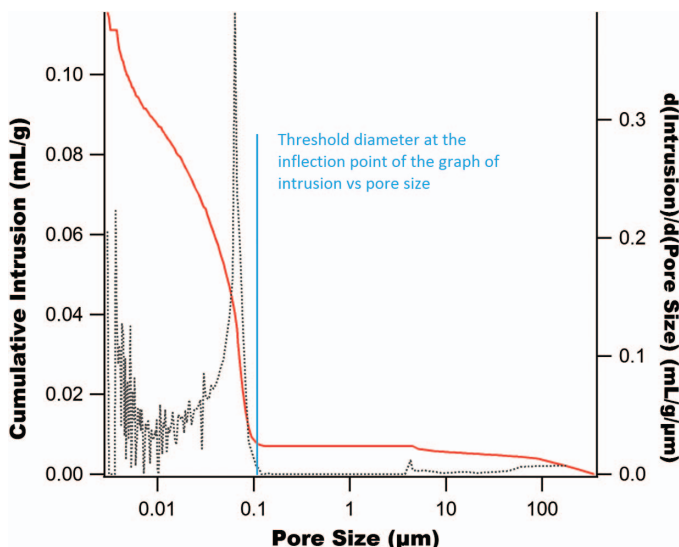


Fig. 14. (Color) Threshold diameter can be determined by finding the inflection point of the intrusion versus size graph for VA-30 specimen.

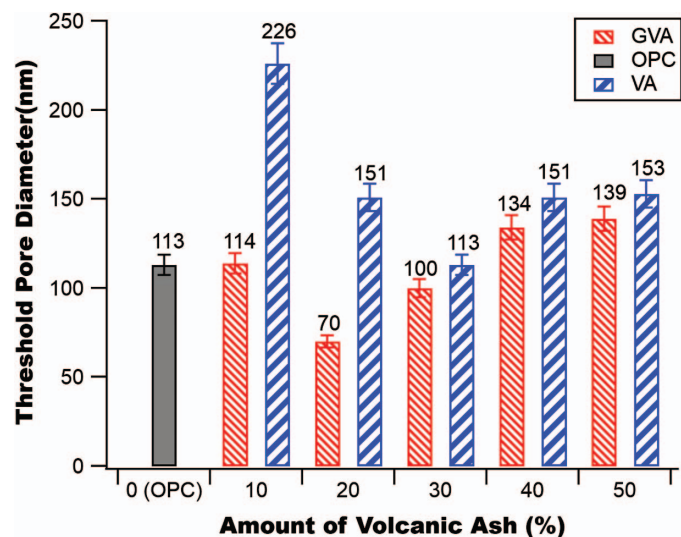


Fig. 15. (Color) Threshold pore diameters for OPC and OPC–volcanic ash samples with two different particle sizes. GVA = mean particle size of $6\text{ }\mu\text{m}$; and VA = mean particle size of $17\text{ }\mu\text{m}$.

increasing VA at 40% or more inclusion of VA. On average, the GVA samples showed 27% reduction in threshold pore diameter when compared with the VA samples. This indicates that grinding the volcanic ash from 17 to $6\text{ }\mu\text{m}$ will provide a greater benefit in the range of 10–30% replacement of OPC with $6\text{-}\mu\text{m}$ volcanic ash.

Porosities calculated using Eq. (1) for each specimen are shown in Fig. 16. It emphasizes that porosity represents the value for the bulk sample and should not be misinterpreted with threshold pore diameter. In general, each GVA sample showed lower porosity compared with its VA counterpart. For GVA samples, porosity decreased when the concentration increased from 10 to 20%, but it gradually increased with amount of volcanic ash at greater than 20% replacement of OPC with volcanic ash. For VA samples, porosity increased from 10 to 20% volcanic ash, decreased from 20 to 30% volcanic ash, and increased with amount of volcanic ash for all samples with greater than 30% volcanic ash. These results suggest that both the particle size and the concentration of the volcanic ash affected the overall porosity of the cement pastes. Effects of size and concentration of volcanic ash on porosity can be interpreted based on the summary of the microstructure

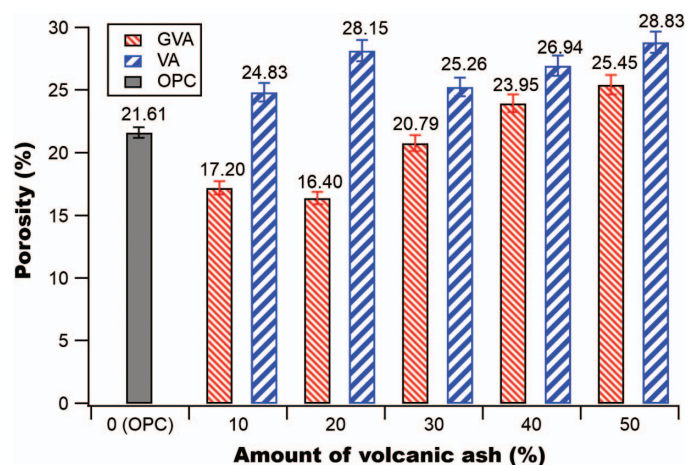


Fig. 16. (Color) Porosity calculated from MIP data.

Table 6. Summary of the results of the microstructure and pore structure evaluation of the hardened cement paste combinations

Characterization technique (scale)	Hardened cement paste prepared with the combination of 17- μm VA and OPC	Hardened cement paste prepared with the combination of 6- μm GVA and OPC
Mechanical properties		
Compressive strength analysis (mm)	Considering the average for all combinations, VA specimens showed ~15% decrease in compressive strength compared with GVA specimens.	All GVA specimens showed higher compressive strength up to 40% replacement of OPC with volcanic ash.
Pore structure characterization		
MIP (nm- μm)	The threshold pore diameters and porosities of each VA sample were greater than GVA and OPC samples. To effectively substitute volcanic ash to OPC, grinding the volcanic ash to finer size leads to benefits in terms of dense pore structure and reduction in porosity.	Each GVA sample had a lower porosity than the corresponding VA counterpart of the same concentration, but of all the VA and GVA samples, only GVA-10, GVA-20, and GVA-30 had a lower porosity than the baseline OPC sample. Reduced porosity due to densification of the matrix was attributed to the secondary C-S-H formation along with calcite, which acted as a pore-filling agent.
Microstructural characterization		
Synchrotron X-ray diffraction (nm)	The specimens demonstrated C-A-S-H led phases such as chabazite-Ca along with tobermorite.	The specimens detected several phases relating to C-S-H (tobermorite) along with calcite, which contributed to higher strength phases when compared to specimens prepared with 17- μm volcanic ash. A majority of the GVA specimens were in the high-calcium regime of C-S-H gels; thus, C-S-H was the dominant phase for strength. The GVA-30, GVA-40, and GVA-50 specimens showed traces of enstatite (crystalline magnesium silicate).
BSE and EDS analysis using ternary phase diagrams (μm)	VA-30 and VA-10 were in high-calcium zone, whereas the rest of the VA and GVA samples were in the medium-calcium zone. VA-30 had the maximum strength, whereas VA-10 had the lowest strength. The data suggest that additional alumina, silica, and calcium from the volcanic ash helped to form secondary C-S-H. No major calcite peaks were detected from VA samples. Mg-based phases (magnesite and dolomites) dominated VA specimens and may have contributed to reduction in compressive strength. C_3S peaks were detected, suggesting some part of the OPC was involved in the initial hydration reaction.	Calcite peaks were detected along with C-S-H phases. Calcite could be attributed to the space-filling capacity, and portlandite along with C-S-H was responsible for higher strength among GVA specimens. C_3S peaks were not detected among GVA samples, suggesting that grinding the volcanic ash to 6 μm allowed the C_3S to react with volcanic ash to form hydration products such as C-S-H and C-A-S-H gels.
Raman spectroscopy (nm- μm)		

characterization shown in Table 6. These data show how grinding the volcanic ash from 17 to 6 μm improves the material by reducing the porosity. OPC can be substituted at a higher concentration when using finer volcanic ash, thus allowing extended use of naturally available materials instead of portland cements.

A summary of the results of microstructure and pore structure of hardened cement paste using a variety of techniques at various length scales (XRD = nanometer; BSE and Raman = micrometer; MIP = nano- to millimeter range; and compression test = macroscale) helps to decipher the effect of natural additives and provides an insight into the basis for developing engineered portland cements (Table 6).

Conclusions

This study provides insight for engineering cements with volcanic ash additives along with guidelines for specific combinations of volcanic ash and OPC. Volcanic ash was ground to two different mean sizes (17 and 6 μm), and its effect as a cement additive on mechanical properties, pore structure, and microstructure was observed in specimens that had been cured for 28 days. Specimens prepared with 6- μm volcanic ash showed higher compressive strength for up to 40% replacement of OPC with volcanic ash. Greater than 30% substitution of 17- μm volcanic ash led to a decrease in strength that could be attributed to the crystalline magnesium silicate (enstatite) and magnesium aluminosilicate phases (cordierite). Microstructure analysis with XRD, BSE/EDS, and

Raman spectroscopy showed that having both secondary C-S-H and calcite resulted in a denser microstructure, and thus a greater strength. Similarly, this work showed that using a smaller sized volcanic ash also resulted in a denser pore structure, and thus a greater compressive strength. In particular, XRD analysis showed that the specimens made of the smaller sized GVA were dominated by C-S-H phases and calcite, which explained why they had a greater strength than the VA specimens. An implication of this study is that engineered volcanic ash is an effective cement additive, and it can be chosen as a partial replacement for other synthetic pozzolan additives for specific industrial applications and criteria.

Acknowledgments

This project was sponsored by the Kuwait Foundation for the Advancement of Sciences. The project was conducted as part of the Kuwait-Massachusetts Institute of Technology (MIT) signature project on sustainability of Kuwait's built environment under the direction of Professor Oral Buyukozturk. Use of the Advanced Photon Source at Argonne National Laboratory was supported by the US Department of Energy, Office of Science, Office of Basic Energy Sciences, under Contract No. DE-AC02-06CH11357. The authors would like to thank 11-BM staff Dr. Saul H. Lapidus and Lynn Ribaud. This work made use of the Materials Research Science and Engineering Centers (MRSEC) Shared Experimental Facilities at MIT, supported by the National Science Foundation under Award No. DMR-1419807. We thank Dr. Charlie Settens

from the Center for Material Science and Engineering (CMSE) from MIT for helping with XRD analysis. We would like to thank Patrick Boisvert for assisting in scanning electron microscopy (SEM) imaging at the CMSE laboratory in MIT. The authors are thankful to Douglas Shattuck, Vern Roberston, and Masateru Shibata from JEOL USA Inc. for helping with the BSE microscopy and EDS analysis.

References

- Alper, A. 2012. *Phase diagrams 6-V: Materials science and technology*. London, UK: Elsevier.
- ASTM. 2014. *Standard practice for mechanical mixing of hydraulic cement pastes and mortars of plastic consistency*. ASTM C305-14. West Conshohocken, PA: ASTM.
- ASTM. 2016. *Standard test method for compressive strength of hydraulic cement mortars (using 2-in. or [50-mm] cube specimens)*. ASTM C109. West Conshohocken, PA: ASTM.
- Barker, A. P. 1989. "An electron optical examination of zoning in blastfurnace slag hydrates. I: Slag cement pastes at early ages." *Adv. Cem. Res.* 2 (8): 171–179. <https://doi.org/10.1680/adcr.1989.2.8.171>.
- Bayuseno, A. P., and W. W. Schmahl. 2010. "Understanding the chemical and mineralogical properties of the inorganic portion of MSWI bottom ash." *Waste Manage.* 30 (8–9): 1509–1520. <https://doi.org/10.1016/j.wasman.2010.03.010>.
- Bernal, S. A., M. C. G. Juenger, X. Ke, W. Matthes, B. Lothenbach, N. De Belie, and J. L. Provis. 2016. "Characterization of supplementary cementitious materials by thermal analysis." *Mater. Struct.* 50 (26): 1–13. <https://doi.org/10.1617/s11527-016-0909-2>.
- Brew, D. R. M., and F. P. Glasser. 2005. "Synthesis and characterisation of magnesium silicate hydrate gels." *Cem. Concr. Res.* 35 (1): 85–98. <https://doi.org/10.1016/j.cemconres.2004.06.022>.
- Celik, K., M. D. Jackson, M. Mancio, C. Meral, A. H. Emwas, P. K. Mehta, and P. J. M. Monteiro. 2014. "High-volume natural volcanic pozzolan and limestone powder as partial replacements for portland cement in self-compacting and sustainable concrete." *Cem. Concr. Compos.* 45: 136–147. <https://doi.org/10.1016/j.cemconcomp.2013.09.003>.
- Chindaprasirt, P., C. Jaturapitakkul, and T. Sinsiri. 2005. "Effect of fly ash fineness on compressive strength and pore size of blended cement paste." *Cem. Concr. Compos.* 27 (4): 425–428. <https://doi.org/10.1016/j.cemconcomp.2004.07.003>.
- Conjeaud, M., and H. Boyer. 1980. "Some possibilities of Raman microprobe in cement chemistry." *Cem. Concr. Res.* 10 (1): 61–70. [https://doi.org/10.1016/0008-8846\(80\)90052-6](https://doi.org/10.1016/0008-8846(80)90052-6).
- Diamond, S. 2000. "Mercury porosimetry: An inappropriate method for the measurement of pore size distributions in cement-based materials." *Cem. Concr. Res.* 30 (10): 1517–1525. [https://doi.org/10.1016/S0008-8846\(00\)00370-7](https://doi.org/10.1016/S0008-8846(00)00370-7).
- Engelsen, C. J., H. A. van der Sloot, G. Wibetoe, G. Petkovic, E. Stoltenberg-Hansson, and W. Lund. 2009. "Release of major elements from recycled concrete aggregates and geochemical modelling." *Cem. Concr. Res.* 39 (5): 446–459. <https://doi.org/10.1016/j.cemconres.2009.02.001>.
- Fisher, R. V., and H.-U. Schmincke. 1984. "Alteration of volcanic glass." *Chap. 12 in Pyroclastic rocks*, 312–345. Berlin, Germany: Springer.
- Garcia-Lodeiro, I., A. Palomo, A. Fernández-Jiménez, and D. E. Macphee. 2011. "Compatibility studies between N-A-S-H and C-A-S-H gels. Study in the ternary diagram Na₂SiO₃-CaO-O." *Cem. Concr. Res.* 41 (9): 923–931. <https://doi.org/10.1016/j.cemconres.2011.05.006>.
- Gardner, L. J., S. A. Bernal, S. A. Walling, C. L. Corkhill, J. L. Provis, and N. C. Hyatt. 2015. "Characterisation of magnesium potassium phosphate cements blended with fly ash and ground granulated blast furnace slag." *Cem. Concr. Res.* 74: 78–87. <https://doi.org/10.1016/j.cemconres.2015.01.015>.
- Herfort, D., and B. Lothenbach. 2015. "Ternary phase diagrams applied to hydrated cement." In *A practical guide to microstructural analysis of cementitious materials*, 485–502. Boca Raton, FL: CRC Press.
- Hewlett, P. 2003. *Lea's chemistry of cement and concrete*. New York, NY: Elsevier.
- Hipedinger, N. E., A. N. Scian, and E. F. Aglietti. 2002. "Magnesia-phosphate bond for cold-setting cordierite-based refractories." *Cem. Concr. Res.* 32 (5): 675–682. [https://doi.org/10.1016/S0008-8846\(01\)00725-6](https://doi.org/10.1016/S0008-8846(01)00725-6).
- Hossain, K. M. A. 2003. "Blended cement using volcanic ash and pumice." *Cem. Concr. Res.* 33 (10): 1601–1605. [https://doi.org/10.1016/S0008-8846\(03\)00127-3](https://doi.org/10.1016/S0008-8846(03)00127-3).
- Hossain, K. M. A., and M. Lachemi. 2006. "Development of volcanic ash concrete: Strength, durability and micro-structural investigations." *ACI Mater. J.* 103 (1): 11–17.
- Hossain, K. M. A., and M. Lachemi. 2007. "Strength, durability and micro-structural aspects of high performance volcanic ash concrete." *Cem. Concr. Res.* 37 (5): 759–766. <https://doi.org/10.1016/j.cemconres.2007.02.014>.
- Husain, A., K. Kupwade-Patil, A. F. Al-Aibani, and M. F. Abdulsalam. 2017. "In situ electrochemical impedance characterization of cement paste with volcanic ash to examine early stage of hydration." *Constr. Build. Mater.* 133: 107–117. <https://doi.org/10.1016/j.conbuildmat.2016.12.054>.
- Jackson, M. D., S. R. Mulcahy, H. Chen, Y. Li, Q. Li, P. Cappelletti, and H.-R. Wenk. 2017. "Phillipsite and Al-tobermorite mineral cements produced through low-temperature water-rock reactions in Roman marine concrete." *Am. Mineral.* 102 (7): 1435–1450. <https://doi.org/10.2138/am-2017-5993CCBY>.
- Jackson, M. D., G. Vola, D. Všianský, J. Oleson, B. Scheetz, C. Brandon, and R. Hohlfelder. 2012. "Cement microstructures and durability in ancient roman seawater concretes." In *Historic mortars*, edited by J. Válek, J. J. Hughes, and C. J. W. P. Groot, 49–76. Dordrecht, Netherlands: Springer.
- Krauskopf, K. B., and D. K. Bird. 1995. *Introduction to geochemistry*. New York, NY: McGraw-Hill.
- Kupwade-Patil, K., A. F. Al-Aibani, M. F. Abdulsalam, C. Mao, A. Bumajdad, S. D. Palkovic, and O. Büyüköztürk. 2016a. "Microstructure of cement paste with natural pozzolanic volcanic ash and portland cement at different stages of curing." *Constr. Build. Mater.* 113: 423–441. <https://doi.org/10.1016/j.conbuildmat.2016.03.084>.
- Kupwade-Patil, K., M. Tyagi, C. M. Brown, and O. Büyüköztürk. 2016b. "Water dynamics in cement paste at early age prepared with pozzolanic volcanic ash and ordinary portland cement using quasielastic neutron scattering." *Cem. Concr. Res.* 86: 55–62. <https://doi.org/10.1016/j.cemconres.2016.04.011>.
- Leonelli, C., E. Kamseu, D. N. Boccaccini, U. C. Melo, A. Rizzuti, N. Billong, and P. Miselli. 2007. "Volcanic ash as alternative raw materials for traditional vitrified ceramic products." *Adv. Appl. Ceram.* 106 (3): 135–141. <https://doi.org/10.1179/174367607X159329>.
- Lloyd, R., J. Provis, and J. J. Deventer. 2009. "Microscopy and micro-analysis of inorganic polymer cements. 1: Remnant fly ash particles." *J. Mater. Sci.* 44 (2): 608–619. <https://doi.org/10.1007/s10853-008-3077-0>.
- Luke, K., H. F. W. Taylor, and G. L. Kalousek. 1981. "Some factors affecting formation of truscottite and xonotlite at 300–350°C." *Cem. Concr. Res.* 11 (2): 197–203. [https://doi.org/10.1016/0008-8846\(81\)90060-0](https://doi.org/10.1016/0008-8846(81)90060-0).
- Masmoudi, R., K. Kupwade-Patil, A. Bumajdad, and O. Büyüköztürk. 2017. "In situ Raman studies on cement paste prepared with natural pozzolanic volcanic ash and ordinary portland cement." *Constr. Build. Mater.* 148: 444–454. <https://doi.org/10.1016/j.conbuildmat.2017.05.016>.
- Massazza, F. 2002. "Properties and applications of natural pozzolanas." In *Structure and performance of cements*, edited by J. Bensted, and J. P. Barnes, 326–352. London: Spon Press.
- Matschei, T., B. Lothenbach, and F. P. Glasser. 2007. "The role of calcium carbonate in cement hydration." *Cem. Concr. Res.* 37 (4): 551–558. <https://doi.org/10.1016/j.cemconres.2006.10.013>.
- Mindess, S. 2000. "The strength and fracture of concrete: The role of the calcium hydroxide." In *Proc., Workshop on the Role of Calcium Hydroxide in Concrete*, 143–154. Holmes Beach, FL.
- Moon, J., S. Bae, K. Celik, S. Yoon, K.-H. Kim, K. S. Kim, and P. J. M. Monteiro. 2014. "Characterization of natural pozzolan-based geopolymeric binders." *Cem. Concr. Compos.* 53: 97–104. <https://doi.org/10.1016/j.cemconcomp.2014.06.010>.

- Neville, A. M. 2011. *Properties of concrete*. Essex, England: Prentice Hall.
- Nied, D., K. Enemark-Rasmussen, E. L'Hopital, J. Skibsted, and B. Lothenbach. 2016. "Properties of magnesium silicate hydrates (M-S-H)." *Cem. Concr. Res.* 79: 323–332. <https://doi.org/10.1016/j.cemconres.2015.10.003>.
- Pauly, B. D., P. Schiffman, R. A. Zierenberg, and D. A. Clague. 2011. "Environmental and chemical controls on palagonitization." *Geochem. Geophys. Geosyst.* 12 (12): Q12017. <https://doi.org/10.1029/2011GC003639>.
- Puertas, F., M. Palacios, H. Manzano, J. S. Dolado, A. Rico, and J. Rodríguez. 2011. "A model for the C-A-S-H gel formed in alkali-activated slag cements." *J. Eur. Ceram. Soc.* 31 (12): 2043–2056. <https://doi.org/10.1016/j.jeurceramsoc.2011.04.036>.
- Sbordoni-Mora, L. 1981. "Les matériaux des enduits traditionnels." In *Mortars, cements and grouts used in the conservation of historic buildings/Mortiers, ciments et coulis utilisés dans la conservation des bâtiments historiques*, 375–383. Rome, Italy: International Centre for the Study of the Preservation and Restoration of Cultural Property.
- Scrivener, K. L., and R. J. Kirkpatrick. 2008. "Innovation in use and research on cementitious material." *Cem. Concr. Res.* 38 (2): 128–136. <https://doi.org/10.1016/j.cemconres.2007.09.025>.
- Skalny, J. P., J. Gebauer, and I. Odler. 2001. *Materials science of concrete: Calcium hydroxide in concrete*. Westerville, OH: American Ceramic Society.
- Slanička, Š. 1991. "The influence of fly ash fineness on the strength of concrete." *Cem. Concr. Res.* 21 (2–3): 285–296. [https://doi.org/10.1016/0008-8846\(91\)90010-F](https://doi.org/10.1016/0008-8846(91)90010-F).
- Snellings, R., G. Mertens, and J. Elsen. 2012. "Supplementary cementitious materials." *Rev. Mineral. Geochem.* 74 (1): 211–278. <https://doi.org/10.2138/rmg.2012.74.6>.
- Sorrell, C. A. 1960. "Reaction sequence and structural changes in cordierite refractories." *J. Am. Ceram. Soc.* 43 (7): 337–343. <https://doi.org/10.1111/j.1151-2916.1960.tb13667.x>.
- Taylor, H. F. W. 1997. *Cement chemistry*. 2nd ed. London, UK: Thomas Telford.
- Walton, A. W., P. Schiffman, and G. L. Macpherson. 2005. "Alteration of hyaloclastites in the HSDP 2 Phase 1 drill core: 2. Mass balance of the conversion of sideromelane to palagonite and chabazite." *Geochem. Geophys. Geosyst.* 6 (9): Q09G19. <https://doi.org/10.1029/2004GC000903>.
- Wang, J., B. H. Toby, P. L. Lee, L. Ribaud, S. M. Antao, C. Kurtz, M. Ramanathan, R. B. V. Dreele, and M. A. Beno. 2008. "A dedicated powder diffraction beamline at the advanced photon source: Commissioning and early operational results." *Rev. Sci. Instrum.* 79: 085105. <https://doi.org/10.1063/1.2969260>.
- Zhang, T., L. J. Vandeperre, and C. R. Cheeseman. 2014. "Formation of magnesium silicate hydrate (M-S-H) cement pastes using sodium hexametaphosphate." *Cem. Concr. Res.* 65: 8–14. <https://doi.org/10.1016/j.cemconres.2014.07.001>.